Author/s:
Howitt, G;Melatos, A

Title:
Antiglitches in accreting pulsars from superfluid vortex avalanches

Date:
2022-07-01

Citation:
Howitt, G. & Melatos, A. (2022). Antiglitches in accreting pulsars from superfluid vortex avalanches. Monthly Notices of the Royal Astronomical Society, 514 (1), pp.863-874. https://doi.org/10.1093/mnras/stac1358.

Persistent Link:
https://hdl.handle.net/11343/320438

Monthly Notices of the ROYAL ASTRONOMICAL SOCIETY

MNRAS **514,** 863–874 (2022) https://doi.org/10.1093/mnras/stac1358
Advance Access publication 2022 May 20

Antiglitches in accreting pulsars from superfluid vortex avalanches

G. Howitt [1,2]★ and A. Melatos[1,3]

[1]*School of Physics, University of Melbourne, Parkville, Victoria, 3010 Australia*
[2]*OzGrav, Australian Research Council Centre of Excellence for Gravitational Wave Discovery, University of Melbourne, Victoria, 3010 Australia*
[3]*Peter MacCallum Cancer Centre, Melbourne, Victoria, 3000 Australia*

Accepted 2022 May 10. Received 2022 May 4; in original form 2021 October 28

ABSTRACT

Three sudden spin-down events, termed 'antiglitches', were recently discovered in the accreting pulsar NGC 300 ULX-1 by the *Neutron Star Interior Composition Explorer* mission. Unlike previous antiglitches detected in decelerating magnetars, these are the first antiglitches recorded in an accelerating pulsar. One standard theory is that pulsar spin-up glitches are caused by avalanches of collectively unpinning vortices that transfer angular momentum from the superfluid interior to the crust of a neutron star. Here, we test whether vortex avalanches are also consistent with the antiglitches in NGC 300 ULX-1, with the angular momentum transfer reversed. We perform N-body simulations of up to 5×10^3 pinned vortices in two dimensions in secularly accelerating and decelerating containers. Vortex avalanches routinely occur in both scenarios, propagating inwards and outwards, respectively. The implications for observables, such as size and waiting time statistics, are considered briefly.

Key words: dense matter – stars: neutron – pulsars: general.

1 INTRODUCTION

Around 10 per cent of known pulsars experience sudden changes in spin frequency known as glitches. Typically, glitches occur in isolated pulsars and are observed as a near-instantaneous increase $\Delta\nu$ in frequency ν that interrupts the stars' steady spin-down caused by electromagnetic braking (Lyne, Graham-Smith & Graham-Smith 2006). Glitches occur at random times with intervals from weeks to years and with fractional sizes spanning $10^{-10} \lesssim \Delta\nu/\nu \lesssim 10^{-5}$. Most glitches are discovered through a secular drift in the phase residuals of pulsar timing experiments, which can be undone by including a step change in the frequency ν, often followed by a transient increase in the pulsar's spin-down rate $\dot{\nu}$ (Wang et al. 2000). The epoch and size of the glitch are determined by least-squares fitting to a phase-connected timing model between the observations. Other detection techniques also exist, such as the hidden Markov scheme described in Melatos et al. (2020). Palfreyman et al. (2018) observed a glitch in the Vela pulsar in real time, and Ashton et al. (2019) used Bayesian parameter estimation to track the frequency evolution during the glitch. Glitches do not occur in isolated electromagnetically braking pulsars exclusively. Spin-up glitches have also been observed in accretion-powered pulsars (Serim et al. 2017) and magnetars (Dib, Kaspi & Gavriil 2008).

Antiglitches, i.e. sudden *decreases* in the spin frequency, are rarer than spin-up glitches. They have been observed in accretion-powered pulsars (Ray et al. 2019) and magnetars (Dib et al. 2008). The situation in magnetars is complicated: Antiglitches and spin-up glitches can occur in the same object, e.g. 1E 2259+586 (Kaspi et al. 2003; Archibald et al. 2013; Younes et al. 2020), they are accompanied sometimes by radiative changes in the pulse profile and X-ray flux (Dib et al. 2008; Dib & Kaspi 2014), and they may be triggered or modified by internal reorganization of the magnetic field instead of electromagnetic braking (Garcia & Ranea-Sandoval 2015; Mastrano, Suvorov & Melatos 2015). We therefore elect not to model magnetar antiglitches in this paper. In contrast, antiglitches in accretion-powered pulsars present a simpler physical phenomenon. They are essentially the reverse of glitches in rotation-powered pulsars – that is, impulsive spin-down events which occur when the star accelerates secularly under the action of an accretion torque. They are the focus of this work.

Recent observations from the *Neutron Star Interior Composition Explorer* (NICER) mission on the International Space Station (Gendreau et al. 2016) reported three spin-down glitches in the accreting pulsar NGC 300 ULX-1 (Ray et al. 2019). Ultraluminous X-ray sources (ULXs) are extragalactic X-ray-bright point sources with super-Eddington luminosities, some of which (though not all) host neutron stars (King & Lasota 2016; Kaaret, Feng & Roberts 2017). NGC 300 ULX-1 is a high-mass X-ray binary in the nearby galaxy NGC 300, which is visible only in outburst (Monard 2010; Binder et al. 2011). Carpano et al. (2018) detected pulsations in NGC 300 ULX-1, unambiguously identifying it as a neutron star, and a NICER campaign in 2018 timed this object daily for ≈100 d before it became too faint. During this interval, Ray et al. (2019) constructed a coherent timing model over several contiguous data segments of ≈10 d each, measuring $\dot{\nu} = 4.3 \times 10^{-10}$ Hz s^{-1} (spin-up). Ray et al. (2019) also measured an antiglitch with $\Delta\nu/\nu = -4.4 \times 10^{-4}$ at MJD 58243 and a second antiglitch with $\Delta\nu/\nu = -5.5 \times 10^{-4}$ at MJD 58265. A third antiglitch with $\Delta\nu/\nu = -7 \times 10^{-4}$ occurred at MJD 58334; however, a phase-coherent timing model could not be constructed around this event as the X-ray flux dropped. No spectral changes were detected around any of the glitches; however, this finding is not conclusive due to the inherent variability of NGC 300 ULX-1. Unlike the antiglitching magnetar 1E 2259+586, NGC 300 ULX-1 has

★ E-mail: gawhowitt@gmail.com

$\dot{\nu} > 0$ due to accretion. It is worth noting that not all accreting pulsars spin up (Bildsten et al. 1997; Long, Romanova & Lovelace 2005). Another ULX, M82-X2, experienced a spin-up glitch (Bachetti et al. 2020). Interestingly, this glitch occurred while M82-X2 was observed to be spinning down, despite previous observations measuring it to be spinning up (Bachetti et al. 2014).

A popular theoretical explanation of glitches is that they are caused by superfluid vortex avalanches (Anderson & Itoh 1975; Warszawski & Melatos 2011; Haskell & Melatos 2015), although alternatives such as starquakes are also viable (Ruderman 1976; Alpar et al. 1996; Middleditch et al. 2006; Chugunov & Horowitz 2010; Giliberti & Cambiotti 2022). Quantized vortices in the superfluid inner crust are postulated to be pinned metastably at nuclear lattice sites or magnetic flux tubes locked to the crust, until the spin-down-driven crust-superfluid lag exceeds a threshold, and the vortices unpin collectively via knock-on processes (Warszawski & Melatos 2011) and migrate radially outwards en masse, transferring angular momentum from the superfluid to the crust (Anderson & Itoh 1975). This mechanism has been explored extensively for spin-up glitches (Haskell & Melatos 2015); however, there is every reason a priori to think that it applies in reverse to antiglitches too, such as those in accreting pulsars, with vortices migrating inwards instead of outwards (Ray et al. 2019).

In this paper we test this idea rigorously, by solving the equations of motion self-consistently for $\sim 10^4$ vortices using an N-body solver calibrated against traditional spin-up glitches in a decelerating container (Howitt, Melatos & Haskell 2020). The simulations demonstrate that spinning up the container results in avalanches where vortices move inwards, causing antiglitches. The paper is organized as follows. In Section 2, we provide some background on the vortex avalanche model for spin-up and spin-down glitches. In Section 3, we describe the mathematical framework of the N-body point vortex model and its equations of motion. We also outline the numerical solver, including a new algorithm for adding additional vortices as the angular velocity of the container increases. In Section 4, we present the results of simulations of vortex avalanches leading to antiglitches and compare the results with traditional spin-up glitches, when the torque on the container reverses sign. In Section 5, we discuss idealizations inherent to the model. In Section 6, we apply the results to observations of glitches and the antiglitches in NGC 300 ULX-1 and contrast its behaviour with that observed in magnetars.

2 SUPERFLUID VORTEX AVALANCHES

To orient the reader, we begin with a brief review of the standard picture of vortex avalanches for traditional spin-up glitches in Section 2.1. We then explain qualitatively in Section 2.2 how the same mechanism is expected to operate in reverse for antiglitches and foreshadow some subtle differences between the two 'directions' of vortex migration. These qualitative descriptions are then tested quantitatively with the N-body solver (Howitt et al. 2020) in Section 3 onwards.

2.1 Spin-up glitches in isolated pulsars

In a superfluid, rotation is supported by the formation of an array of vortices with quantized circulation (Onsager 1949; Feynman 1955). The inner crust of a neutron star is expected to contain $\sim 10^{15}$ vortices (Baym, Pethick & Pines 1969; Alpar 1977). At length-scales much greater than the intervortex separation, the rotational characteristics of a superfluid mimic solid body rotation (Osborne 1950). For a container rotating with angular velocity Ω, the number of vortices N_v within radius R is determined by the Feynman condition (Feynman 1955):

$$N_\mathrm{v}\kappa = \Omega R^2, \tag{1}$$

where $2\pi\kappa$ is the quantum of circulation.

Equation (1) implies that vortices move outwards as the star spins down due to electromagnetic braking. However, the outwards motion is frustrated by nuclear lattice sites or magnetic flux tubes, which pin vortices, leading to differential rotation between the viscous component of the star (which is coupled to the crust) and the inviscid superfluid component (Alpar 1977). The lag between the components builds until a (local) threshold is exceeded and individual vortices unpin. The unpinned vortices trigger knock-on unpinning of nearby vortices, e.g. via proximity or acoustic effects, leading to a vortex avalanche (Warszawski, Melatos & Berloff 2012). The motion of the vortices transfers angular momentum from the superfluid to the crust or vice versa, depending on the direction in which they move. If the vortices move radially outwards on average, the superfluid spins down, and the crust spins up (Pethick & Smith 2001).

2.2 Antiglitches in accreting pulsars

Equation (1) also implies that if the star spins up (e.g. by accretion), then vortices tend to migrate inwards, as N_v/R^2 increases. Under these circumstances, the scenario in Section 2.1 runs in reverse. Pinning at nuclear sites or magnetic flux tubes frustrates the inwards migration; vortices unpin collectively in an avalanche mediated by knock-on processes, when the crust-superfluid lag exceeds a threshold; vortices move radially inwards during the avalanche; and the angular momentum of the superfluid increases, while the angular momentum of the crust decreases. The result is an antiglitch with $\Delta\nu < 0$. The process by which vortices nucleate at the outer boundary and enter the superfluid, as the superfluid spins up, is approximately but not exactly a reversal of the process by which they exit the superfluid, as the superfluid spins down (Stagg et al. 2016).

3 POINT VORTEX DYNAMICS

When the intervortex separation is much greater than the vortex core radius, the quantum mechanical structure of the vortex cores can be ignored and vortices are treated as point-like filamentary features in the velocity field obeying classical hydrodynamics (Bustamante & Nazarenko 2015). In the absence of external forces such as pinning or dissipation, the velocity $\mathrm{d}\mathbf{x}/\mathrm{d}t$ of a vortex at $\mathbf{x}(t)$ is equal to the bulk fluid velocity at $\mathbf{x}(t)$ induced by the other vortices, which can be computed directly from the vorticity distribution. In the system studied here, the vortices are also influenced by interactions with impurities, the container boundary, and a viscous fluid component which corotates with the container.

In this paper, we consider an array of point vortices in a circular container with cylindrical symmetry. The restriction to two dimensions assumes that the vortex filaments are infinitely long, rigid, and aligned parallel to the rotation axis. This assumption ignores the potentially important three-dimensional (3D) dynamics of vortex tangles and vortex tension (Peralta et al. 2006; Drummond & Melatos 2017, 2018; Mongiovì, Russo & Sciacca 2017; Haskell, Antonopoulou & Barenghi 2020) but is a necessary simplification in order to simulate $N_\mathrm{v} \gtrsim 10^3$ vortices in order for collective avalanche motion to be observable.

3.1 Equations of motion

In a reference frame rotating with angular velocity Ω, the position of a vortex at Cartesian coordinates, $(x_i,\ y_i)$, evolves according to

$$\frac{\mathrm{d}}{\mathrm{d}t}\begin{pmatrix} x_i \\ y_i \end{pmatrix} = \mathcal{R}_\phi \begin{pmatrix} v_{i,x} \\ v_{i,y} \end{pmatrix}, \tag{2}$$

with

$$v_{i,x} = -\sum_{j\neq i} \frac{\kappa\, y_{ij}}{r_{ij}^2} + \sum_{j=1}^{N_\mathrm{v}} \frac{\kappa\, y_{ij,\mathrm{image}}}{r_{ij,\mathrm{image}}^2} + \Omega y_i - \sum_k \frac{\partial V(\mathbf{x}_i - \mathbf{x}_k)}{\partial y_i} \tag{3}$$

$$v_{i,y} = \sum_{j\neq i} \frac{\kappa\, x_{ij}}{r_{ij}^2} - \sum_{j=1}^{N_\mathrm{v}} \frac{\kappa\, x_{ij,\mathrm{image}}}{r_{ij,\mathrm{image}}^2} - \Omega x_i + \sum_k \frac{\partial V(\mathbf{x}_i - \mathbf{x}_k)}{\partial x_i}. \tag{4}$$

In equations (3) and (4), $2\pi\kappa$ is the quantum of circulation and we define $\mathbf{x}_{ij} = \mathbf{x}_i - \mathbf{x}_j = (x_{ij}, y_{ij})$ to be the displacement between vortices at $\mathbf{x}_i$ and $\mathbf{x}_j$, with $r_{ij} = |\mathbf{x}_{ij}|$. We also define $\mathbf{x}_{ij,\mathrm{image}} = \mathbf{x}_i - \mathbf{x}_{j,\mathrm{image}} = (x_{ij,\mathrm{image}},\ y_{ij,\mathrm{image}})$ to be the displacement between a vortex at $\mathbf{x}_i$ and the image vortex of a vortex at $\mathbf{x}_j$, with $r_{ij,\ \mathrm{image}} = |\mathbf{x}_{ij,\ \mathrm{image}}|$. Image vortices enforce a no-penetration boundary condition of the superfluid at the boundary in the dissipation-free regime (Schwarz 1985). The function $V(\mathbf{x} - \mathbf{x}_k) = -V_0 \exp[-(\mathbf{x} - \mathbf{x}_k)^2/2\xi^2]$ describes the attractive pinning potential with depth V_0 and characteristic width ξ due to a pinning site at $\mathbf{x}_k$. In equation (2), the term $\mathcal{R}_\phi$ describes rotation of the velocity vector through a 'dissipation angle' ϕ, whose value relates to the strength of interaction between the inviscid and viscous components of the superfluid (Campbell & Ziff 1979; Sedrakian 1995). We use a dimensionless coordinate system, where κ and the fundamental length unit both equal unity. All other quantities, such as time and velocity, are defined through these quantities. A more detailed explanation of equations (2)–(4) is provided in Howitt et al. (2020).

3.2 *N*-Body solver

In this paper, we use the same Python code for solving equations (2)–(4) described in Howitt et al. (2020).

Simulations are initialized by creating an ensemble of N_v point vortices within a circular container of radius R. The initial positions are drawn at random from a uniform spatial distribution. The container contains a square grid of pinning sites with grid spacing a, pinning depth V_0, and characteristic width ξ. The initial angular velocity of the container $\Omega(t = 0)$ is determined from equation (1). At each time-step, we compute the velocity of all vortices from equations (2)–(4) and step forward in time using an adaptive time-step Runge–Kutta–Cash–Karp scheme. If any vortices leave the container, their circulation is set to zero and their contribution to equations (2)–(4) is ignored.

After each time-step, we evolve the angular velocity of the container Ω_C by solving

$$\frac{\mathrm{d}\Omega_\mathrm{C}}{\mathrm{d}t} = N_\mathrm{ext} - I_\mathrm{rel}\frac{\mathrm{d}\Omega_\mathrm{S}}{\mathrm{d}t}. \tag{5}$$

Here, N_ext is the external torque divided by the container moment of inertia I_C, and we set $I_\mathrm{rel} = I_\mathrm{S}/I_\mathrm{C} = 1$ in all simulations described in this paper, where I_S is the moment of inertia of the superfluid treated notionally as a rigid body. The angular velocity of the superfluid Ω_S is determined by the configuration of the vortex array (Fetter, Hohenberg & Pincus 1966; Howitt et al. 2020). We assume the change in angular momentum of the vortex array is transferred conservatively to the container (Pethick & Smith 2001).

In order to test whether the vortex code can produce antiglitches similar to those in NGC 300 ULX-1, we perform simulations on pinned vortices in an accelerating container. In this scenario, vortices tend to move toward the centre of the container in order to maintain the Feynman condition (1). Therefore, as the container spins up, new vortices must be added, otherwise an annular region around the boundary becomes depleted (unphysically) of vortices. This issue does not arise in Howitt et al. (2020), where only decelerating containers are considered. In terrestrial superfluids, it is observed that vortices enter the system at the outer boundary, where the density is lowest, and vortex nucleation is favoured energetically (Donnelly 1991; Stagg et al. 2016). For this paper, we modify the code to include a simple algorithm which inserts a new vortex at $r = 0.999R$ and at a random angular coordinate, whenever Ω increases by κ/R^2 since the last vortex was added.

4 ANTIGLITCH SIMULATIONS

We perform a suite of numerical experiments to investigate whether antiglitches in an accelerating container are simply the time-reversed analogue of glitches during spin-down. The system parameters for the simulations are, cf. section 5.1 of Howitt et al. (2020): $R = 10$, $\Delta t = 0.1T_0$ (where $T_0 = 2\pi R^2/N_\mathrm{v}\kappa$ is the initial rotation period of the container), $I_\mathrm{rel} = 1$, $V_0 = 2000$, $a = 10^{-2}R$ (i.e. there are approximately 10 pinning sites for each vortex initially in the simulation), $\xi = 10^{-3}R$, and $\phi = 0.1$ rad. Here, I_rel is the moment of inertia of the container divided by the nominal moment of inertia of the superfluid, approximated for this purpose as a uniformly rotating rigid body, as in the standard two-component model of a neutron star (Baym et al. 1969).

We initialize the vortices by drawing their positions from a random spatial distribution. We then evolve the system without spin-up/spin-down or container feedback until all vortices are pinned, which we define as when no vortices move a distance more than the pinning-site separation a between successive time-steps.

We perform four numerical experiments, described below and summarized in Table 1.

(i) Spin-up from the pinned initial state with $N_\mathrm{ext} = 10^{-3}\Omega_0/T_0$ for 2×10^5 time-steps, or $0 \leq t/T_0 \leq 2 \times 10^4$.

(ii) Spin-down from the pinned initial state with $N_\mathrm{ext} = -10^{-3}\Omega_0/T_0$ for 2×10^5 time-steps, or $0 \leq t/T_0 \leq 2 \times 10^4$.

(iii) We resume experiment I where it left off at $t/T_0 = 2 \times 10^4$ and continue for $2 \times 10^4 < t/T_0 \leq 4 \times 10^4$ with $N_\mathrm{ext} = -10^{-3}\Omega_0/T_0$, i.e. the sign of the torque is reversed.

(iv) We resume experiment II where it left off at $t/T_0 = 2 \times 10^4$ and continue for $2 \times 10^4 < t/T_0 \leq 4 \times 10^4$ with $N_\mathrm{ext} = 10^{-3}\Omega_0/T_0$.

We use the same initial vortex configuration for both experiments I and II. Experiments III and IV use the state of the vortex array at $t = 2 \times 10^4 T_0$ in experiments I and II, respectively, as their initial condition.

We describe the avalanche dynamics of antiglitches in experiment I in Section 4.1. We compare the probability distribution functions of the glitch/antiglitch size and waiting time probability density functions (PDFs) from experiments I and II in Section 4.2. We find that the size and waiting time PDFs from experiments I and II are significantly different. We explore possible causes for this difference in Section 4.3 and in Appendix A, which also includes discussion of experiments III and IV. Finally, we vary the parameters V_0, a, N_ext, and ϕ in the same way as in section 5.4 of Howitt et al. (2020) in order to explore how each parameter affects the properties of antiglitches. The results are presented in Section 4.4.

Table 1. Summary of numerical experiments described in Section 4 showing initial and final numbers of vortices $N_{v,\,\mathrm{i}}$ and $N_{v,\,\mathrm{f}}$, initial and final container angular velocities Ω_i and Ω_f, number of glitches N_glitches, external torque N_ext, and the time span of each simulation.

	Experiment I	Experiment II	Experiment III	Experiment IV
$N_{v,\,\mathrm{i}}$	1943	1943	2361	1498
$\Omega_\mathrm{i}/\Omega_0$	1	1	1.27	0.74
$N_{v,\mathrm{f}}$	2361	1498	1998	1888
$\Omega_\mathrm{f}/\Omega_0$	1.27	0.74	0.99	1.01
N_glitches	176	101	116	166
N_ext	$10^{-3}\Omega_0/T_0$	$-10^{-3}\Omega_0/T_0$	$-10^{-3}\Omega_0/T_0$	$10^{-3}\Omega_0/T_0$
Time span	$0 \le t/T_0 \le 2\times10^4$	$0 \le t/T_0 \le 2\times10^4$	$2\times10^4 < t/T_0 \le 4\times10^4$	$2\times10^4 < t/T_0 \le 4\times10^4$

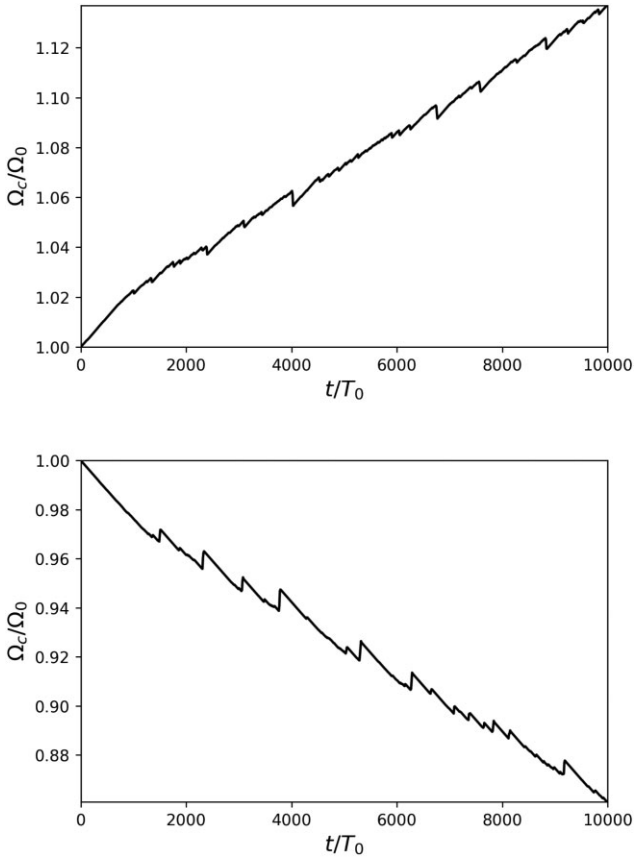

Figure 1. Container angular velocity Ω_C, normalized by its initial value Ω_0, as a function of time for $t < 10^4 T_0$. Top panel: Experiment I. Bottom panel: Experiment II.

4.1 Avalanche dynamics

Fig. 1 shows the evolution of the angular velocity of the container Ω_C, normalized by its initial value Ω_0 during experiment I (top panel) and experiment II (bottom panel). For clarity, we show only $t < 10^4 T_0$. The behaviour of Ω_C in Fig. 1 is qualitatively similar in both experiments I and II. The steady spin-up/spin-down is punctuated by abrupt spin-down/spin-up events of varying size at random times.

Observing the vortex motion directly, we see that antiglitches in an accelerating container occur in much the same way as glitches in a decelerating container, but in reverse. Single vortices unpin and move inwards, causing knock-on unpinning of other vortices which also move inwards. Fig. 2 depicts the motion of vortices during the largest antiglitch in experiment I, which occurs at $t \approx 4000 T_0$ and has $\Delta\Omega_\mathrm{C}/\Omega_0 = -5.9\times10^{-3}$, cf. figs 5 and 9 in Howitt et al. (2020). The top five panels show how the avalanche progresses, with Ω_C versus t shown in the bottom panel. The moving vortices are indicated by red dots, with their positions in the previous 20 time-steps indicated by black (fading to grey) tracers. The stationary vortices are indicated by grey dots.

(i) At $t/T_0 = 4012$, two vortices unpin in the lower right quadrant of the container. Another vortex unpins in the bottom-left region close to the boundary. Neither unpinning event noticeably changes the evolution of Ω_C.

(ii) At $t/T_0 = 4016$, more vortices unpin in the lower right quadrant through proximity knock-on and move towards the centre of the container. The other unpinned vortex in the bottom-left region remains unpinned, but does not knock-on other vortices. The inwards motion of the unpinned vortices changes the sign of $\dot{\Omega}_\mathrm{C}$.

(iii) At $t/T_0 = 4020$, the avalanche continues in the lower right quadrant. As well as the vortices unpinned by proximity knock-on, some vortices unpin closer to the boundary than the original unpinned vortices, and move inwards towards the depleted region left by the first batch of unpinned vortices. The other unpinned vortex in the bottom-left region has re-pinned. $\dot{\Omega}_\mathrm{C}$ remains negative.

(iv) At $t/T_0 = 4030$, the unpinned vortices begin to re-pin. As they do so, their trajectory bends clockwise as opposed to the more radial motion earlier in the avalanche. $\dot{\Omega}_\mathrm{C}$ begins to level off.

(v) At $t/T_0 = 4039$, almost all of the vortices that unpinned in the avalanche have re-pinned, and the steady increase of Ω_C resumes.

Fig. 2 demonstrates that if vortex avalanches are responsible for glitches in electromagnetically braking pulsars then the same mechanism can cause antiglitches in accretion-powered pulsars in principle.

4.2 Size and waiting time statistics

While the physical mechanism causing antiglitches and glitches may be the same, the statistical properties of the glitches and antiglitches in equivalent simulations differ. Generally, antiglitches are smaller in magnitude and more frequent than the glitches. The smallest antiglitch in experiment I has $|\Delta\Omega_\mathrm{C}|/\Omega_\mathrm{C} = 1.1\times10^{-6}$ and the largest antiglitch has $|\Delta\Omega_\mathrm{C}|/\Omega_\mathrm{C} = 5.9\times10^{-3}$, while the smallest glitch in experiment II has $|\Delta\Omega_\mathrm{C}|/\Omega_\mathrm{C} = 4.7\times10^{-6}$ and the largest glitch has $|\Delta\Omega_\mathrm{C}|/\Omega_\mathrm{C} = 8.7\times10^{-3}$. There are 176 antiglitches and 101 glitches.

Fig. 3 shows kernel density estimates (KDEs) of the glitch/antiglitch size and waiting time PDFs in experiments I and II. For sizes, we look at the PDF of the absolute value $|\Delta\Omega_\mathrm{C}|/\Omega_\mathrm{C}$ for ease of comparison. The size and waiting time PDFs for both experiments I and II have similar shapes; however, the distributions for antiglitches are steeper. A two-sample Kolmogorov–Smirnov (KS) test returns a

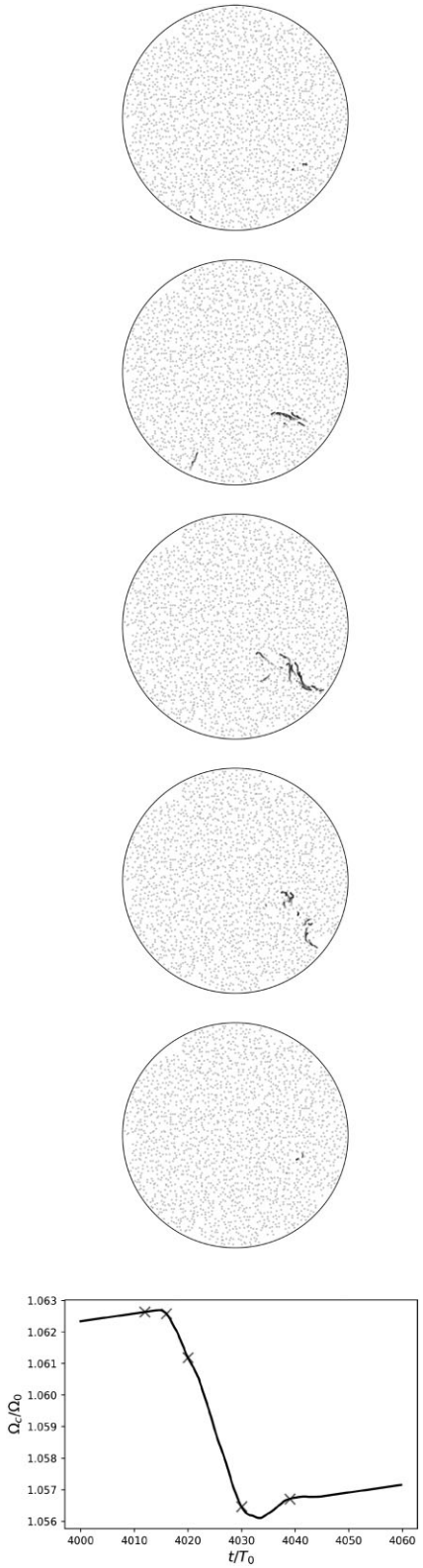

Figure 2. Vortex motion during an antiglitch. Top five panels are snapshots from experiment I at $t/T_0 = 4012, 4016, 4020, 4030$, and 4039 (top to bottom). Grey dots show stationary vortices; red dots show vortices that have moved in the previous time-step; and black (fading to grey) tracers show the positions of the moving vortices for the 20 previous time-steps in the rotating frame of the container. Bottom panel: Container angular velocity Ω_C versus time t. Snapshots from the top five panels are marked with blue crosses.

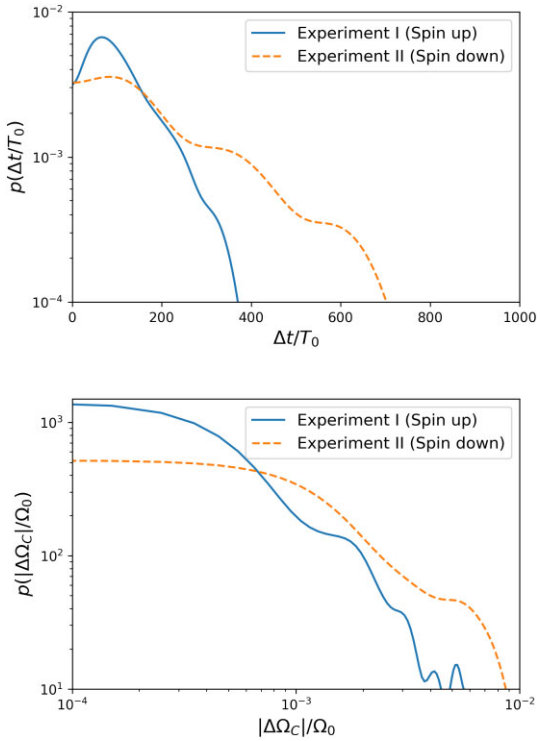

Figure 3. KDEs of the glitch waiting time (top panel) and size (bottom panel) PDFs for experiment I (blue curve) and experiment II (orange dashed curve).

p-value of 2.8×10^{-4} for the waiting times and 4.4×10^{-3} for the sizes. This means that the null hypothesis that the PDFs are the same for each simulation is rejected for both the sizes and waiting times.

4.3 Why do spin-up and spin-down differ?

While initially surprising, the result that antiglitches tend to be smaller and more frequent can be at least partially explained by the interplay between local and global dynamics of the pinned vortex array. The argument presented in this section is reasonable but not definitive, because the far-from equilibrium dynamics are too complex for an analytic proof. We explore other possible causes of the glitch/antiglitch size/waiting time discrepancy in Appendix A below.

The angular momentum of the superfluid is given by (Fetter et al. 1966; Howitt et al. 2020)

$$L_S = k \sum_{i=1}^{N_v} (R^2 - r_i^2), \tag{6}$$

where k is a constant with units of kg s^{-1} and r_i is the radial coordinate of a vortex. If a vortex moves from r_i to $r_i + \Delta r$, the change in the angular velocity of the container, by conservation of angular momentum, is given by

$$\Delta\Omega_C \propto \Delta r^2 + 2 r_i \Delta r, \tag{7}$$

i.e. $|\Delta\Omega_C|$ is less for vortices moving inwards than outwards by the same radial distance.

In Fig. 4, we show the joint PDF of the mean distance travelled by vortices in each avalanche, $\langle|\Delta r|\rangle$, in experiments I and II, as well as the number of vortices that move a distance $\Delta r > a$, denoted by $N_{\rm move}$. Fig. 4 shows that the PDFs of $\langle|\Delta r|\rangle$ and $N_{\rm move}$ are

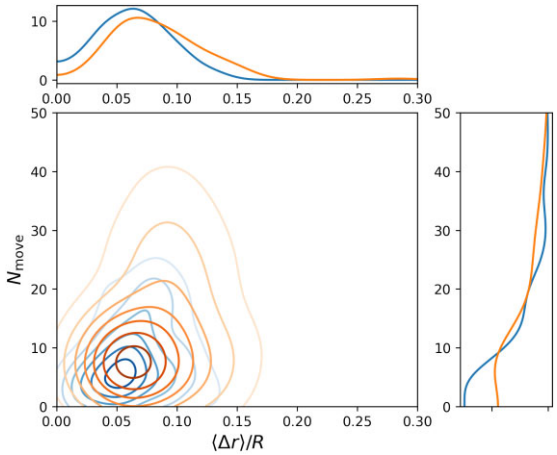

Figure 4. Joint PDF of mean distance travelled by vortices in avalanches $\langle \Delta r \rangle$ and number of vortices in each avalanche $N_{\rm move}$ for experiment I (blue contours) and experiment II (orange contours). 1D projections of the individual PDFs are shown in the margins.

similar in experiments I and II. Avalanches involve the same number of vortices moving the same radial distance before re-pinning, on average. The reduced angular momentum transfer from inwards-moving avalanches is therefore primarily responsible for the reduced size of antiglitches.

This is only half the story, however. One might wonder why the inwards-moving vortices in experiment I do not travel further in order to transfer as much angular momentum as in experiment II. When a vortex unpins, and where it subsequently re-pins, are determined by the local stress at the location of the vortex (Haskell & Melatos 2016). In hydrodynamical descriptions of superfluid dynamics (e.g. Hall & Vinen 1956; Barenghi, Donnelly & Vinen 1983), this stress S is proportional to the velocity lag between a viscous 'normal' fluid component with velocity $\mathbf{v}_n$ and an inviscid superfluid component with velocity $\mathbf{v}_s$, i.e. $S \propto |\mathbf{v}_s - \mathbf{v}_n|$. Let us consider a single vortex at radial coordinate r which moves to $r + \Delta r$. Ignoring the local contributions to the superfluid velocity from the vortices in its immediate neighbourhood (an appropriate approximation given that we are trying to explain only the average behaviour of many vortices across many avalanches), we can take both the superfluid and normal fluid velocity fields to be azimuthal. The normal fluid corotates with the container, so one has $v_n = \Omega_{\rm C} r$. The superfluid velocity, by the Feynman condition is $v_s = \kappa N(r)/r$, where $N(r) \propto r^2$ is the number of vortices within a circle of radius r centred on the origin. Thus the change in the stress for a vortex moving from r to $r + \Delta r$ is

$$S = S(r + \Delta r) - S(r) \propto \Delta r. \tag{8}$$

The symmetry of equation (8) with respect to Δr explains why vortices move the same distance on average in avalanches in experiments I and II, while the asymmetry in equation (7) explains why antiglitches are smaller in magnitude than glitches.

The fact that antiglitches are smaller than glitches does not mean that the differential rotation is greater in accretion-powered pulsars. In both experiments I and II, after the onset of avalanches the magnitude of the spin-up/spin-down rate (averaged over the entire simulation) reduces to approximately half its initial value, as shown in Fig. 1, reflecting the fact that avalanches couple the superfluid moment of inertia ($I_{\rm rel} = 1$) to that of the crust. While antiglitches are smaller than glitches, the corresponding reduced waiting times mean that they transfer the same amount of angular momentum over a long-enough time-scale.

It is unlikely that the statistical asymmetry between glitches and antiglitches is observable in pulsars. Superfluid vortices likely pin only in the inner crust/outer core region at $r \gtrsim 0.9R$, and the typical glitch size of $\Delta\Omega_{\rm C}/\Omega_{\rm C} \sim 10^{-6}$ implies $\Delta r \ll r_i$, so the second term in equation (7) dominates. It may however be observable in terrestrial experiments with superfluids or Bose–Einstein condensates, which necessarily involve fewer vortices than the $\sim 10^{15}$ in pulsars and stronger torques.

As well as the simulations with $N_{\rm v} = 2000$ presented here, we also performed a suite of comparable simulations on systems with $500 \leq N_{\rm v} \leq 5000$. The results from these simulations are qualitatively similar to those discussed in this section and are not displayed for brevity.

4.4 Model variations

As in Howitt et al. (2020), we run a suite of spin-up simulations varying several of the input parameters, namely the pinning strength V_0, the pinning site separation a, the dissipation angle ϕ, and the external spin-up rate $N_{\rm ext}$. In each case, we keep all the other parameters at their same value as in the default simulation. As well as the default values given at the beginning of Section 4, we run simulations with $V_0 = 1000$ and $V_0 = 4000$; $a = 0.025R$ and $a = 0.005R$, corresponding to pinning site-vortex abundance ratios of ≈ 1 and ≈ 100, respectively; $\phi = 0.01$ rad and $\phi = 0.5$ rad; and $N_{\rm ext} = -5 \times 10^{-4}\Omega_0/T_0$ and $N_{\rm ext} = -2 \times 10^{-3}\Omega_0/T_0$.

In Table 2, we show the qualitative effect of adjusting each of the parameters on the mean absolute glitch size $\langle |\Delta\Omega_{\rm C}| \rangle$ and mean waiting time $\langle \Delta t \rangle$ in both the spin-up simulations in this paper and (by way of comparison) the spin-down simulations from Howitt et al. (2020).

Table 2 shows that the antiglitches have a similar response to parameter variations as glitches. As expected, our findings are largely the same as in Howitt et al. (2020). Increasing the pinning strength V_0 makes vortices harder to unpin, so fewer avalanches occur. When vortices unpin they are more stressed, leading to more knock-on and hence larger glitch sizes. Increasing the pinning site separation a (i.e. decreasing the pinning site density) increases the waiting time in the spin-down case without affecting the glitch size, while no effect is observed in spin-up simulations. The nominal difference between the spin-up and spin-down simulations versus a is marginal and may be related to the inability of the glitch-finding algorithm to resolve small avalanches involving few vortices. Changing the dissipation angle ϕ from the default value $\phi = 0.1$ rad in either direction results in more, smaller glitches and antiglitches. The cause is complicated and discussed in detail in section 5.4 of Howitt et al. (2020). Increasing/decreasing the external torque $|N_{\rm ext}|$ increases/decreases the number of avalanches because vortices accumulate stress faster/slower, but the avalanche sizes are unaffected.

We also study forward and backward cross-correlations between sizes and waiting times for all of our model variations, cf. section 5.5 in Howitt et al. (2020). For the default parameters (experiment I), the Spearman rank coefficient for the forward correlation, i.e. the correlation between size and subsequent waiting time is $\rho_+ = 0.54$ compared to $\rho_+ = 0.44$ for experiment II. The backward correlation, i.e. the correlation between size and the preceding waiting time, is $\rho_- = -0.10$ for experiment I compared to $\rho_- = 0.03$ for experiment II. We refrain from including correlation coefficients from all simulations here, as the results are basically the same as

Table 2. Effect of varying simulation parameters (first column) on vortex avalanche statistics: mean waiting time $\langle \Delta t/T_0 \rangle$ between antiglitches (second column) and glitches (third column); and mean size $\langle |\Delta\Omega_C| \rangle$ of antiglitches (fourth column) and glitches (fifth column). Symbols + (−) indicate that $\langle \Delta t \rangle$ or $\langle |\Delta\Omega_C| \rangle$ increases (decreases) relative to the default value in Section 4.1 as the parameter in first column increases; and '.' indicates no consistent effect.

Parameter	$\langle \Delta t/T_0 \rangle$ (spin-up)	$\langle \Delta t/T_0 \rangle$ (spin-down)	$\langle \lvert\Delta\Omega_C\rvert \rangle$ (spin-up)	$\langle \lvert\Delta\Omega_C\rvert \rangle$ (spin-down)
V_0	+	+	+	+
a	.	+	.	.
ϕ	.	.	.	.
$\lvert N_{ext}\rvert$	−	−	.	.

those shown in Howitt et al. (2020). We see weak but statistically significant forward correlations for all parameter variations except weak dissipation, and we see no statistically significant backward correlations. This stands in contrast to the measured correlations in glitching pulsars, where few significant forward correlations are observed (Melatos, Howitt & Fulgenzi 2018).

5 IDEALIZATIONS IN THE POINT VORTEX MODEL

The point vortex model described in Section 3 makes a number of approximations and simplifications. It is not intended to be a fully realistic model of a neutron star, given the many physical and astrophysical uncertainties in the problem. Several of the idealizations involved are discussed thoroughly by Haskell & Melatos (2015) and in section 7 of Drummond & Melatos (2018) in the Gross–Pitaevskii context. In this section, we discuss three issues of special relevance to the point vortex model in this paper: the cylindrical geometry, extrapolation to higher N_v, and the physics of vortex pinning in the presence of magnetic flux tubes.

5.1 Cylindrical geometry

It is natural to ask whether the artificial cylindrical geometry in this paper behaves differently to the spherical geometry expected in a neutron star, at least as far as antiglitch observables are concerned. There are three key issues.

(i) The motion of a neutron star vortex is insensitive to conditions at its endpoints (including the shape of the boundary), because vortices are long and thin. The length of a vortex ($\sim$10 km) is much greater than its diameter ($\sim$10 fm), if the simple Feynman–Onsager picture of a rotating superfluid is applied uncritically to a neutron star (Haskell & Melatos 2015), without allowing for the macroscopic and microscopic imperfections which are likely to exist, e.g. grain boundaries and lattice dislocations in the crust, compositional variations, gravitational stratification, and inhomogeneous superfluid phases. In the simple picture, therefore, the middle of an $\sim$10 km vortex (near the star's equatorial mid-plane) is not affected meaningfully by what happens at the boundaries, where vortices terminate. To an excellent approximation, every vortex terminates at a wall which is perpendicular to its length, i.e. normal at the point of contact, because the radius of curvature of the star ($\sim$10 km) is much greater than the vortex diameter ($\sim$10 fm) and even the vortex separation ($\sim$1 mm). The physical decoupling between most of a vortex and its endpoints is even more pronounced, when the realistic inhomogeneities listed above are considered. One way to visualize this is that Kelvin waves propagating along a vortex from the endpoints encounter many complicated scattering centres and refractive index variations, which cause them to lose 'memory' of the conditions at the boundary. In this sense, point vortices are a better approximation than $\sim$10 km vortices. Their effective (as opposed to nominal) length, which is much less than 10 km, is discussed in point (ii) below.

(ii) Superfluid vortices are not perfectly rigid. Their rigidity is quantified by a stiffness parameter $T_v r_0/(F_{pin} a)$, where T_v is the vortex tension (Hall & Vinen 1956; Barenghi et al. 1983), r_0 is the pinning site radius (roughly equivalent to ξ in our notation), F_{pin} is the characteristic pinning force, and a is the pinning site separation. The stiffness is dimensionless and gives roughly the number of pinning sites across which the vortex moves coherently as a rigid bar (Link & Epstein 1991; Link, Epstein & Baym 1993; Seveso et al. 2016; Tsubota, Fujimoto & Yui 2017). If T_v is relatively low, with $T_v r_0 \lesssim F_{pin} a$, vortex unpinning occurs through single-site breakaway; if T_v is relatively high, with $T_v r_0 \gtrsim F_{pin} a$, vortex unpinning occurs through multisite breakaway (Link & Epstein 1991). Either way we have $T_v r_0/(F_{pin} a) \lesssim 10^2$ according to equation (3.9) in Link et al. (1993), so even the stiffest vortex is rigid on microscopic scales only. Therefore a 10 km long vortex behaves like a 'gas' of $\gtrsim 10^{15}$ independent point vortices, each moving in a plane, as in our simulations, and only a tiny fraction interact with the walls. This is even truer in the realistic case of a polarized vortex tangle, which we do not treat in this paper (Tsubota, Araki & Barenghi 2003; Peralta et al. 2006; Andersson, Sidery & Comer 2007).

(iii) Experiments by Tsakadze & Tsakadze (1980) involving pinned vortices in decelerating containers show spasmodic, glitch-like dynamics for both cylindrical and spherical containers, without much qualitative difference. This is consistent with the hydrodynamic theory in van Eysden & Melatos (2010, 2013) where spherical and cylindrical containers are compared. Geometry does exert a subtle influence on post-glitch recovery time-scales (of order weeks to months), because Ekman circulation occurs differently in cylinders and spheres, but the differences are small and irrelevant to the fast vortex unpinning discussed in this paper, which occurs over $\lesssim |\Omega_S - \Omega_C|^{-1} \sim 1$ s.

5.2 Extrapolation to higher N_v

The simulations in this paper track $N_v \lesssim 10^4$ vortices, compared to $N_v \gtrsim 10^{15}$ vortices in a realistic, accreting neutron star. While this is unavoidable due to computational limitations, it is reasonable to ask to what extent the results of the paper extrapolate to realistic N_v. More work is needed to answer this question definitively, but for now the key criterion seems to be the number of pinning sites per vortex: As long as there are many pinning sites per vortex, extrapolation is relatively safe. Intuitively, if there are many pinning sites in its vicinity, a vortex pins randomly and without preference to any one of them, at a location approximately where it would stand in a regular Abrikosov array, and this holds true

whether there are 10^2 (in a simulation, say) or 10^{18} (in reality) pinning sites in its vicinity. Evidence collected to date from quantum mechanical Gross–Pitaevskii simulations (Warszawski & Melatos 2011; Melatos, Douglass & Simula 2015) and hydrodynamic N-body simulations (Howitt et al. 2020) supports this conclusion, as does the analogy with self-organized critical systems (Jensen 1998); vortex avalanches exhibit the same properties qualitatively, as long as there are more pinning sites than vortices. Encouragingly this is true for a range of pinning sites per vortex (approximately 1 to 10^2), even though the N-body simulations do not include the acoustic knock-on process observed in Gross–Pitaevskii simulations (Warszawski et al. 2012). We are currently investigating analytic approaches to predict glitch scalings versus N_v for $N_\mathrm{v} \gg 1$, but this is a hard problem in far-from-equilibrium statistical mechanics and remains unsolved (Jensen 1998). The number of pinning sites per vortex greatly exceeds unity in a neutron star, whether the pinning occurs at nuclear lattice sites or magnetic flux tubes (see Section 5.3). The dimensional value of quantities like $\langle \Delta t \rangle$ in a neutron star depends on the dimensional value of system-specific quantities like N_ext, of course.

5.3 Magnetic flux tube pinning

The calculations in this paper are largely agnostic about the pinning microphysics, partly because the avalanche dynamics are insensitive to the microphysics (a general property of other self-organized critical systems as well, e.g. sand piles; Jensen 1998) and partly because the microphysics is poorly known (Haskell & Melatos 2015). In this paper, the values of parameters like V_0, a, and ϕ are chosen to broadly reflect the situation expected for pinning at nuclear lattice sites, although their dimensionless values are unrealistic due to numerical limitations; see also Sections 5.1 and 5.1. In this section, for the sake of completeness, we explore briefly how the situation changes for pinning at magnetic flux tubes (Ruderman, Zhu & Chen 1998; Sourie & Chamel 2020). However, we caution that the properties (e.g. number, geometry, and location) of magnetic flux tubes are even less certain in accreting neutron stars than in isolated objects. The global dipole moment is typically $\lesssim 10^4$ times weaker in accreting systems, however the local internal fields can be strong and tangled (Payne & Melatos 2004), and they may or may not be excluded from certain regions (e.g. the outer core) (Viganò et al. 2013; Turlione, Aguilera & Pons 2015).

The pinning microphysics influences vortex avalanches in two main ways, through the pinning site separation a and dissipation angle ϕ. With respect to pinning site separation, in the context of magnetic flux tube pinning, one finds $a = 4 \times 10^{-10} (B/10^{12}\,\mathrm{G})^{-1/2}\,\mathrm{cm}$, where B is the surface magnetic field strength. This is typically greater than the nuclear lattice site separation (∼fm) and flux tube core radius $\approx 5 \times 10^{-13} (n_\mathrm{p}/10^{36}\,\mathrm{cm}^{-3})^{-1/2}\,\mathrm{cm}$, where n_p is the proton number density, but it is smaller than the vortex separation. Hence, flux tube pinning resembles the situation simulated in Section 4 and discussed in Section 5.2, where pinning sites are more abundant than vortices. Although the ratio of pinning sites to vortices satisfies $\lesssim 10^2$ out of computational necessity, Gross–Pitaevskii simulations suggest that the event statistics (e.g. size and waiting-time PDFs) do not change when the ratio increases further (Warszawski & Melatos 2011), consistent with other self-organized critical systems (Jensen 1998). In 2D simulations, or in idealized 3D systems where the flux tubes and vortices are rectilinear and parallel, the number of vortex-flux tube intersections, N_p, termed 'pinned fluxoids' by Sourie & Chamel (2020), equals the number of vortices. However, if the vortices and flux tubes are inclined or tangled, or vortex-fluxoid clusters are formed (Sedrakian & Sedrakian 1995), the number of pinned fluxoids can reach as high as $\sim 10^{13} (B/10^{12}\,\mathrm{G})(\Omega/10^3\,\mathrm{rad\,s^{-1}})^{-1}$ (Sourie & Chamel 2020). Near the upper end of this range, a approaches the nuclear lattice site separation.

With respect to the dissipation angle, one has $\tan\phi = \mathcal{R}$, where $\mathcal{R}$ is the ratio of the drag force to the Magnus force and can be related to the mutual friction coefficient $\mathcal{B} \approx \mathcal{R}$. Sourie & Chamel (2020) calculated $10^{-13} \lesssim \mathcal{B} \lesssim 10^{-3}$ for $1 \leq N_\mathrm{p} \leq 10^{12}$ in the vortex-cluster model (Sedrakian & Sedrakian 1995). The full range implies $\phi \ll 1$, which is the regime simulated in Section 4. Table 2 suggests that the event statistics are insensitive to the exact value of ϕ, as long as it is small, but in fairness we are restricted to $0.01 \leq \phi \leq 0.1$ out of computational necessity and do not probe the lower extremes of the range, viz. $\phi \sim 10^{-13}$, where different behaviour is conceivable.

It is worth noting that the avalanche dynamics are insensitive to the specific, microphysical value of V_0. Self-organized systems tend towards marginal stability: A sand pile fluctuates around a critical slope (Jensen 1998), and likewise the crust-superfluid angular velocity lag in a neutron star fluctuates around a critical value set by the balance of pinning, drag, and Magnus forces. V_0 influences the critical state, i.e. the baseline (and hence quantities like the mean waiting time), but it does not play much role in determining the shapes of the size and waiting-time PDFs, for example. Even though V_0 differs in general for pinning at nuclear lattice sites and magnetic flux tubes, one expects the glitch statistics to be similar, as in other self-organized critical systems (Jensen 1998). One subtle issue, however, is whether the point-like pinning potential in this paper is suitable for flux-tube pinning, which involves a longer range current–current component as well as a short-range density–density component (Srinivasan et al. 1990). It is also unclear whether vortices and flux tubes are tangled or rectilinear when they interact locally; the relevant mesoscopic length-scales cannot be resolved for realistic neutron star parameters by Gross–Pitaevskii and Ginzburg–Landau simulations at present (Drummond & Melatos 2017, 2018).

6 CONCLUSION

We perform simulations of 500–5000 pinned superfluid vortices in accelerating containers. We find that vortex avalanches interrupt the secular increase of the angular velocity to produce antiglitches for a wide range of physical parameters. The results match those demonstrating glitches in decelerating containers from Howitt et al. (2020). The size and waiting time statistics of antiglitches are qualitatively similar to glitches in decelerating containers.

Interestingly, antiglitches in our simulations are smaller and more frequent than glitches, an effect we believe is due to reduced angular momentum transfer between the superfluid and container when vortices move inwards rather than outwards. Such an effect is unlikely to be observable in neutron stars, where one has $\Delta r \ll r_i$ (cf. equation 7), but may be tested in terrestrial experiments on quantized vortices in superfluids and Bose–Einstein condensates.

The antiglitches in NGC 300 ULX-1 suggest a direct analogue with standard glitching pulsars, and hence offer an opportunity to test the applicability of the vortex avalanche model in a new regime. The results in Section 4 and Fig. 2 confirm that, from a microphysical standpoint, inwards-propagating vortex avalanches are a viable explanation for antiglitches in accelerating neutron stars, at least in principle (Ray et al. 2019). Further timing campaigns of accelerating ULX pulsars will hopefully discover more antiglitches in the future, enabling closer comparison to the population of glitches in isolated neutron stars. It is worth noting, however, that these objects are often only observable in outburst, making construction of phase-coherent

timing solutions challenging. Another point worth noting is that not all accreting pulsars are accelerating (Bildsten et al. 1997). This is because the hydromagnetic accretion torque can take either sign depending on the fastness parameter (Ghosh, Lamb & Pethick 1977).

In this paper, we do not seek to model antiglitches in magnetars (Dib et al. 2008). The vortex equations of motion (2)–(4) do not include hydromagnetic forces, which are likely to be important dynamically in magnetars. For example, the kinetic energy per unit volume associated with the crust-superfluid lag, $\rho|\mathbf{v}_s - \mathbf{v}_n|^2 \sim 10^{23}$ erg cm^{-3}, and the comparable pinning energy per unit volume, are much smaller than the magnetic energy per unit volume, $\sim 10^{29}$ erg cm^{-3} (Glampedakis, Andersson & Samuelsson 2011; Mereghetti, Pons & Melatos 2015). However, some of the phenomenology of magnetar antiglitches resembles loosely the results in Section 4, so it is worth generalizing the treatment in this paper to include magnetic fields in future work, e.g. pinning to superconducting magnetic flux tubes (Sidery & Alpar 2009; Drummond & Melatos 2017, 2018). Intriguing examples of magnetar antiglitch phenomenology include the following. Archibald et al. (2013) reported an antiglitch in the magnetar 1E 2259+586. The antiglitch was detected as a discontinuity in the timing model between two observations taken with the *Swift X-ray Telescope* at 2012 April 14 and 2012 April 28. On 2012 April 21, the Fermi Gamma-ray Burst Monitor detected a 36 ms hard X-ray burst from the same object, possibly coincident with the antiglitch. Swift monitoring subsequent to 2012 April 28 measured an increase in the 2–10 keV X-ray flux of a factor of $\approx$2, which then decayed following a power law in time. These associated radiative changes are similar to other glitches in magnetars (Dib et al. 2008; Dib & Kaspi 2014), including one other spin-up glitch in 1E 2259+586 (Kaspi et al. 2003), and unlike radio pulsar glitches. Following the antiglitch, the spin-down rate of the magnetar approximately doubled for $\sim$100 d before returning to its pre-glitch value following a second glitch. The sign of the second glitch is uncertain; Archibald et al. (2013) considered two models, one with an antiglitch followed by a glitch, the other with an antiglitch followed by a second antiglitch, and found no statistical preference for either, but preferred both to a model with only a single antiglitch. More recently, a spin-up and spin-down glitch have been reported in the same object (Younes et al. 2020), both without any associated pulse profile changes or enhanced X-ray flux. As 1E 2259+586 experiences glitch-like timing irregularities of both signs, and is spinning down, it is challenging to reconcile antiglitches in this object with the vortex avalanche model, and it is possible that they are instead due to changes in the internal magnetic field (Garcia & Ranea-Sandoval 2015; Mastrano et al. 2015).

ACKNOWLEDGEMENTS

GH and AM acknowledge support from the Australian Research Council (ARC) through the Centre of Excellence for Gravitational Wave Discovery (OzGrav) (grant number CE170100004) and an ARC Discovery Project (grant number DP170103625).

DATA AVAILABILITY

Simulation data and code used in this paper can be made available upon request by emailing the corresponding author.

REFERENCES

Alpar M. A., 1977, ApJ, 213, 527
Alpar M. A., Pines D., Anderson P. W., Shaham J., 1984, ApJ, 276, 325
Alpar M. A., Chau H. F., Cheng K. S., Pines D., 1996, ApJ, 459, 706
Anderson P. W., Itoh N., 1975, Nature, 256, 25
Andersson N., Sidery T., Comer G. L., 2007, MNRAS, 381, 747
Archibald R. F. et al., 2013, Nature, 497, 591
Ashton G., Lasky P. D., Graber V., Palfreyman J., 2019, Nature Astron., 3, 1143
Bachetti M. et al., 2014, Nature, 514, 202
Bachetti M. et al., 2020, ApJ, 891, 44
Barenghi C. F., Donnelly R. J., Vinen W. F., 1983, J. Low Temp. Phys., 52, 189
Baym G., Pethick C., Pines D., 1969, Nature, 224, 673
Bildsten L. et al., 1997, ApJS, 113, 367
Binder B., Williams B. F., Kong A. K. H., Gaetz T. J., Plucinsky P. P., Dalcanton J. J., Weisz D. R., 2011, ApJ, 739, L51
Bustamante M. D., Nazarenko S., 2015, Phys. Rev. E, 92, 053019
Campbell L. J., Ziff R. M., 1979, Phys. Rev. B, 20, 1886
Carpano S., Haberl F., Maitra C., Vasilopoulos G., 2018, MNRAS, 476, L45
Chugunov A. I., Horowitz C. J., 2010, MNRAS, 407, L54
Dib R., Kaspi V. M., 2014, ApJ, 784, 37
Dib R., Kaspi V. M., Gavriil F. P., 2008, ApJ, 673, 1044
Donnelly R. J., 1991, Quantized Vortices in Helium II. Cambridge Univ. Press, Cambridge, p. 364
Drummond L. V., Melatos A., 2017, MNRAS, 472, 4851
Drummond L. V., Melatos A., 2018, MNRAS, 475, 910
Fetter A. L., Hohenberg P. C., Pincus P., 1966, Phys. Rev., 147, 140
Feynman R. P., 1955, in Gorter C. J., ed., Progress in Low Temperature Physics, Chapt. II, Vol. 1, Elsevier, New York
Garcia F., Ranea-Sandoval I. F., 2015, MNRAS, 449, L73
Gendreau K. C. et al., 2016, Proc. SPIE Conf. Ser. Vol. 9905, Space Telescopes and Instrumentation 2016: Ultraviolet to Gamma Ray. SPIE, Bellingham, p. 99051H
Ghosh P., Lamb F. K., Pethick C. J., 1977, ApJ, 217, 578
Giliberti E., Cambiotti G., 2022, MNRAS, 511, 3365
Glampedakis K., Andersson N., Samuelsson L., 2011, MNRAS, 410, 805
Hall H. E., Vinen W. F., 1956, Proc. R. Soc. A, 238, 215
Haskell B., Melatos A., 2015, Int. J. Mod. Phys. D, 24, 30008
Haskell B., Melatos A., 2016, MNRAS, 461, 2200
Haskell B., Antonopoulou D., Barenghi C., 2020, MNRAS, 499, 161
Howitt G., Melatos A., Haskell B., 2020, MNRAS, 498, 320
Jensen H., 1998, Self-Organized Criticality: Emergent Complex Behavior in Physical and Biological Systems. Cambridge Lecture Notes in Physics. Cambridge Univ. Press, Cambridge
Kaaret P., Feng H., Roberts T. P., 2017, ARA&A, 55, 303
Kaspi V. M., Gavriil F. P., Woods P. M., Jensen J. B., Roberts M. S. E., Chakrabarty D., 2003, ApJ, 588, L93
King A., Lasota J.-P., 2016, MNRAS, 458, L10
Link B. K., Epstein R. I., 1991, ApJ, 373, 592
Link B., Epstein R. I., Baym G., 1993, ApJ, 403, 285
Long M., Romanova M. M., Lovelace R. V. E., 2005, ApJ, 634, 1214
Lyne A., Graham-Smith F., Graham-Smith F., 2006, Pulsar Astronomy. Cambridge Astrophysics. Cambridge Univ. Press, Cambridge
Mastrano A., Suvorov A. G., Melatos A., 2015, MNRAS, 453, 522
Melatos A., Douglass J. A., Simula T. P., 2015, ApJ, 807, 132
Melatos A., Howitt G., Fulgenzi W., 2018, ApJ, 863, 196
Melatos A., Dunn L. M., Suvorova S., Moran W., Evans R. J., 2020, ApJ, 896, 78
Mereghetti S., Pons J. A., Melatos A., 2015, Space Sci. Rev., 191, 315
Middleditch J., Marshall F. E., Wang Q. D., Gotthelf E. V., Zhang W., 2006, ApJ, 652, 1531
Monard L. A. G., 2010, Cent. Bur. Electron. Telegrams, 2289, 1
Mongiovì M. S., Russo F. G., Sciacca M., 2017, MNRAS, 469, 2141
Onsager L., 1949, Il Nuovo Cimento, 6, 279
Osborne D. V., 1950, Proc. Phys. Soc. A, 63, 909
Palfreyman J., Dickey J. M., Hotan A., Ellingsen S., van Straten W., 2018, Nature, 556, 219
Payne D. J. B., Melatos A., 2004, MNRAS, 351, 569
Penttinen A., Stoyan D., Henttonen H. M., 1992, Forest Sci., 38, 806
Peralta C., Melatos A., Giacobello M., Ooi A., 2006, ApJ, 651, 1079

Pethick C. J., Smith H., 2001, Bose-Einstein Condensation in Dilute Gases, Cambridge Univ. Press, Cambridge, p. 414
Ray P. S. et al., 2019, ApJ, 879, 130
Ripley B. D., 1977, J. R. Stat. Soc. B, 39, 172
Ruderman M., 1976, ApJ, 203, 213
Ruderman M., Zhu T., Chen K., 1998, ApJ, 492, 267
Schwarz K. W., 1985, Phys. Rev. B, 31, 5782
Sedrakian A. D., 1995, MNRAS, 277, 225
Sedrakian A. D., Sedrakian D. M., 1995, ApJ, 447, 305
Serim M. M., Şahiner Ş., ćerri-Serim D., Inam S. ć., Baykal A., 2017, MNRAS, 471, 4982
Seveso S., Pizzochero P. M., Grill F., Haskell B., 2016, MNRAS, 455, 3952
Sidery T., Alpar M. A., 2009, MNRAS, 400, 1859
Sourie A., Chamel N., 2020, MNRAS, 493, L98
Srinivasan G., Bhattacharya D., Muslimov A. G., Tsygan A. J., 1990, Curr. Sci., 59, 31
Stagg G. W., Pattinson R. W., Barenghi C. F., Parker N. G., 2016, Phys. Rev. A, 93, 023640
Tsakadze J. S., Tsakadze S. J., 1980, J. Low Temp. Phys., 39, 649
Tsubota M., Araki T., Barenghi C. F., 2003, Phys. Rev. Lett., 90, 205301
Tsubota M., Fujimoto K., Yui S., 2017, J. Low Temp. Phys., 188, 119
Turlione A., Aguilera D. N., Pons J. A., 2015, A&A, 577, A5
van Eysden C. A., Melatos A., 2010, MNRAS, 409, 1253
van Eysden C. A., Melatos A., 2013, J. Fluid Mech., 729, 180
Viganò D., Rea N., Pons J. A., Perna R., Aguilera D. N., Miralles J. A., 2013, MNRAS, 434, 123
Wang N., Manchester R. N., Pace R. T., Bailes M., Kaspi V. M., Stappers B. W., Lyne A. G., 2000, MNRAS, 317, 843
Warszawski L., Melatos A., 2011, MNRAS, 415, 1611
Warszawski L., Melatos A., Berloff N. G., 2012, Phys. Rev. B, 85, 104503
Younes G., Ray P. S., Baring M. G., Kouveliotou C., Fletcher C., Wadiasingh Z., Harding A. K., Goldstein A., 2020, ApJ, 896, L42

APPENDIX A: STATISTICAL DISCREPANCY BETWEEN GLITCHES AND ANTIGLITCHES

Here, we explore and discard some plausible alternative explanations for the discrepancy in event statistics between glitches and antiglitches discussed in Section 4.3. In Section A1, we look at whether it is due to the differing values of N_v in experiments I and II. In Section A2, we look at where in the container avalanches originate. In Section A3, we test for spatial correlations in the distribution of pinned vortices. In Section A4, we look at whether it is due to perturbations to the vortex array caused by the addition of vortices in spin-up simulations. None of our investigations reveal an obvious cause.

A1 Time-reversed simulations

Both experiments I and II begin with the same initial vortex configuration, but in experiment I N_v increases from 1943 at $t = 0$ to 2361 at $t/T_0 = 2 \times 10^4$, while in experiment II N_v decreases to 1498 by $t/T_0 = 2 \times 10^4$. In general, we do not expect a difference in N_v of this magnitude to affect the statistics of the sizes and waiting times. However, to investigate the possibility that this may be the source of the differences in the PDFs between the two simulations, we run time-reversed simulations of each experiment. In experiment III, we use the state of the vortex array from experiment I at $t = 2 \times 10^4 T_0$ as the initial condition and run for $2 \times 10^4 \leq 4 \times 10^4$ with $N_{ext} = -10^{-3}\Omega_0/T_0$. In experiment IV, we use the state of the vortex array from experiment II at $t = 2 \times 10^4 T_0$ as the initial condition and run for $2 \times 10^4 \leq 4 \times 10^4$ with $N_{ext} = 10^{-3}\Omega_0/T_0$. The initial and final values of N_v and Ω_C are shown in Table 1. The evolution of the angular velocity Ω_C in all experiments is shown in Fig. A1.

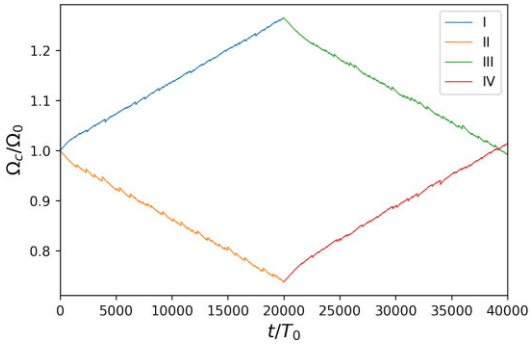

Figure A1. Angular velocity Ω_C versus time for experiments I (blue curve), II (orange curve), III (green curve), and IV (red curve).

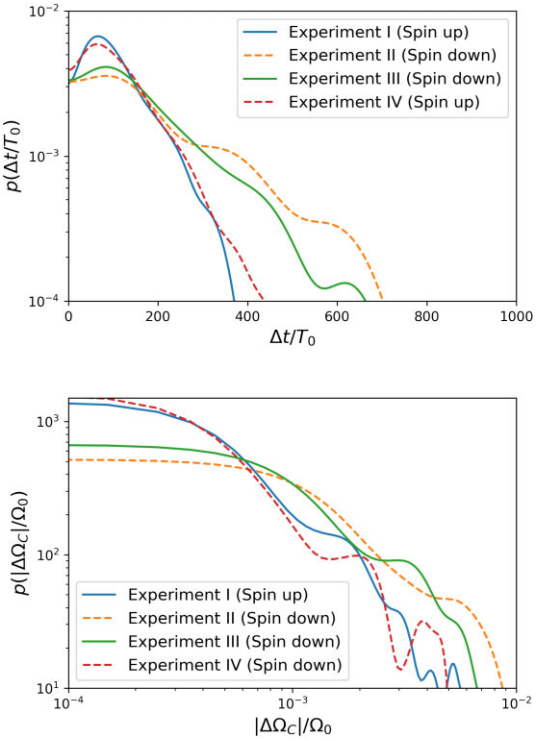

Figure A2. KDEs of the glitch size and waiting time PDFs for experiments I (blue curve), II (orange dashed curve), III (green curve), and IV (red dashed curve).

The latter figure shows that after changing the sign of the torque, the system undergoes a short period of steady spin-down before avalanches begin again, now with the opposite sign as in the initial simulation. Experiment III has 116 glitches, and experiment IV has 166 antiglitches.

If the discrepancy in size and waiting time PDFs seen in Fig. 3 is due to the difference in N_v, then we expect that the size and waiting time PDFs of the torque-reversed spin-up/spin-down simulations should be closer to the spin-up/spin-down simulations they extend rather than the initial simulations with the same torque. The KDEs for the size and waiting time PDFs for all four experiments are shown in Fig. A2. Fig. A2 shows that the simulations with the same sign torque are most similar to one another. To quantify this result, Table A1 shows the p-values from a two-sample KS test for all pairwise combinations of the spin-up, spin-down, and reversed torque simulations. Table A1 shows that the null hypothesis that the glitch

Table A1. *P*-values from a two-sample KS test for glitch and antiglitch sizes $|\Delta\Omega_C|/\Omega_0$ and waiting time $\Delta t/T_0$ from experiments I–IV. The KS test is performed for all pairwise combinations of the four experiments.

	Experiment I		Experiment II		Experiment III		Experiment IV	
	$\lvert\Delta\Omega_C\rvert/\Omega_0$	$\Delta t/T_0$	$\lvert\Delta\Omega_C\rvert/\Omega_0$	$\Delta t/T_0$	$\lvert\Delta\Omega_C\rvert/\Omega_0$	$\Delta t/T_0$	$\lvert\Delta\Omega_C\rvert/\Omega_0$	$\Delta t/T_0$
Experiment I	–		4.4×10^{-3}	2.9×10^{-4}	8.8×10^{-3}	6.4×10^{-3}	0.91	0.94
Experiment II	–		–		0.72	0.33	1.4×10^{-3}	1.3×10^{-3}
Experiment III	–		–		–		5.9×10^{-3}	0.059

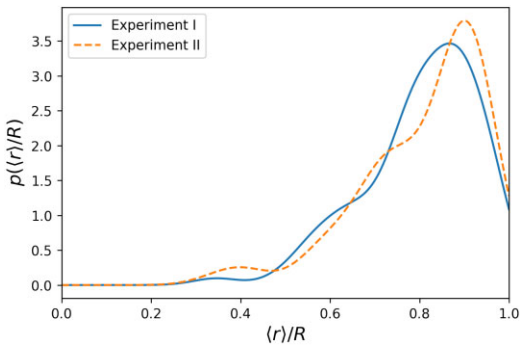

Figure A3. KDE of the PDF of mean starting radial coordinate $\langle r\rangle$ of vortices involved in avalanches in spin-up (blue curve) and spin-down (orange dashed curve).

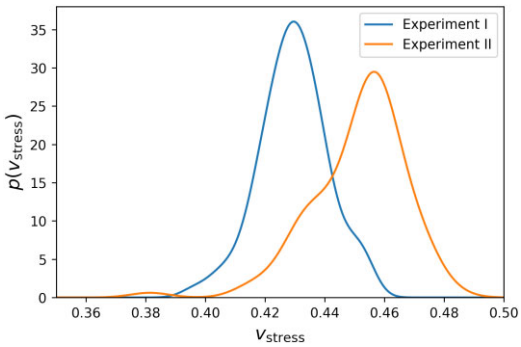

Figure A4. PDFs of vortex-averaged pinning stress $v_{\rm stress}$ in experiments I (blue curve) and II (orange curve), sampled at glitch epochs.

populations are drawn from the same distribution is rejected with high probability for the pairs I/III and II/IV. The null hypothesis is not rejected for the simulations with the same sign of the torque, the pairs I/IV and II/III. The results in Fig. A2 and Table A1 confirm that spin-up and spin-down are not simply time-reversed analogues, and that the difference between the PDFs for glitches and antiglitches is not due to the difference in $N_{\rm v}$ at the beginning or the end of the simulations.

A2 Avalanche locations

In spin-up simulations vortices are continually added near the boundary. This may lead to a bias for avalanches to begin at $r \approx R$. To examine whether such a bias exists, for each glitch and antiglitch in experiments I and II we identify the vortices which move $\Delta r > a$ during the avalanche. We record the radial coordinate of each vortex in the avalanche at the beginning of the avalanche and compute the mean $\langle r\rangle$ for each avalanche. Fig. A3 shows the PDF of $\langle r/R\rangle$ for both the spin-up and spin-down simulations. The PDFs are similar for glitches and antiglitches. This indicates that the discrepancy between the size and waiting time distributions is not due to where vortices unpin.

A3 Stress and spatial correlations

We now look at the distribution of stress in experiments I and II. We parametrize the stress of a vortex as $v_{i,\rm stress} = |\mathbf{v}_{i,\rm induced} - \mathbf{\Omega}_C \times \mathbf{x}_i|/\max|\mathbf{v}_{\rm pin}|$ where $\mathbf{v}_{i,\rm induced}$ is the velocity contribution from the first two terms in equations (3) and (4) and $\max|\mathbf{v}_{\rm pin}| = V_0\xi e^{-1/2}$ is the maximum velocity contribution from a Gaussian pinning site with depth V_0 and characteristic width ξ. A vortex always unpin for $v_{i,\rm stress} > 1$, though it may unpin at lower values. Howitt et al. (2020) found that stress is evenly distributed throughout the container and remains at $\langle v_{\rm stress}\rangle \approx 0.45$ for the duration of a simulation, and that glitches do not substantially reduce the amount of stress in the system even temporarily, e.g. the stress fluctuates by ≈ 10 per cent in the immediate aftermath of a glitch.

Fig. A4 shows the PDF of the vortex-averaged value of $v_{\rm stress}$ at each of the glitch epochs for experiments I and II, i.e. we compute the stress of all vortices at each glitch epoch and take the average over the array.

Fig. A4 shows that the vortices in experiment II are under more stress prior to glitches than in experiment I. The mean value of $v_{\rm stress}$ (averaged across the glitch epochs) is 0.43 in experiment I and 0.45 in experiment II. This result on its own does not necessarily explain the differences between the size and waiting time PDFs in experiments I and II. It may in fact be the case that the smaller, more frequent avalanches in experiment I are the cause of the lower average stress rather than a consequence.

We also test whether there is a difference in spatial clustering of vortices in experiments I and II using Ripley's *K*-function (Ripley 1977). The empirical *K*-function is defined as

$$\hat{K}(r) = \frac{A}{N_{\rm v}(N_{\rm v}-1)} \sum_{i=1}^{N_{\rm v}} \sum_{j=1, j\neq i}^{N_{\rm v}} \mathbf{1}\{r_{ij} \leq r\} e_{ij}, \tag{A1}$$

where A is the area of the observation window, $\mathbf{1}\{r_{ij} \leq r\}$ is an indicator function that returns 1 if $r_{ij} \leq r$ and 0 otherwise, and e_{ij} is an edge-correction term. The *K*-function can be considered a measure of the amount of clustering on a length-scale r. In the case of a Poisson point process (i.e. an uncorrelated spatial distribution), the *K*-function can be determined analytically as $K(r) = \pi r^2$. A point process that has $\hat{K}(r) > \pi r^2$ implies clustering of the points on the length-scale r, and $\hat{K}(r) < \pi r^2$ implies anticlustering. Fig. A5 shows $\hat{K}(r)$ for experiments I and II. Equation (A1) is computed for each experiment at every glitch epoch and averaged in time with three standard deviation error bars. Fig. A5 shows that there is no difference between $\hat{K}(r)$ for experiments I and II, and that both are consistent with a Poisson point process. An extension to the Ripley's *K*-function for marked point processes (such as the vortex coordinates marked by the value of $v_{\rm stress}$) exists, called the mark-weighted point process (Penttinen, Stoyan & Henttonen 1992). We also compute this

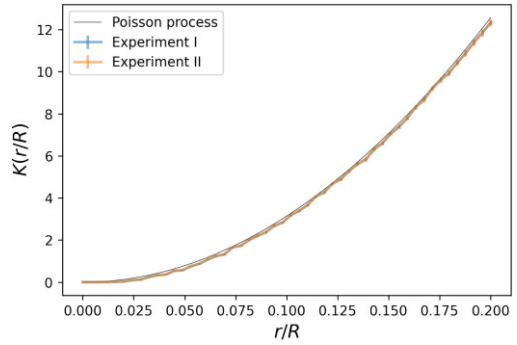

Figure A5. Ripley's K-function for experiment I (blue curve with error bars) and experiment II (orange curve with error bars). Also shown is the theoretical value for a Poisson process $K_{\rm Poisson}(r) = \pi r^2$ (grey curve).

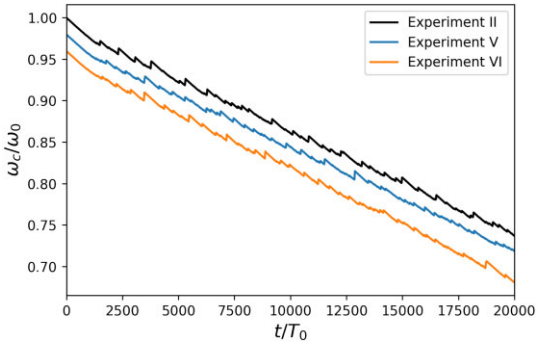

Figure A6. Container angular velocity versus time for experiment II (black curve), experiment V (blue curve), and experiment VI (orange curve). Results for experiments V and VI are offset vertically for clarity.

on the data from experiments I and II and find nearly identical results to those shown in Fig. A5. We find no evidence of spatial correlations in the spatial distributions of vortices or the distributions of stress in either experiment.

A4 Vortex wandering

One obvious difference between experiments I and II is that in experiment I vortices are continually added to the container while in experiment II $N_{\rm v}$ remains constant except during avalanches, when some vortices move out past the container boundary. As shown in Table 1, during experiment I the rate at which vortices are added is several times larger than the rate at which glitches occur. It is possible that the addition of vortices at random angular positions near $r = R$ perturbs the quasi-equilibrium of the pinned vortex array and triggers avalanches. If this is the case, we expect that an analogous process in the spin-down case should increase the glitch rate.

To test this hypothesis, we perform two further numerical experiments where we perturb the vortex array at the same cadence that vortices are added in experiments I and IV. In experiment V, every time $\Omega_{\rm C}$ decreases by κ/R^2 we choose a vortex at random and move it in a randomly chosen direction (horizontal or vertical) by a distance equal to the pinning lattice spacing a. In experiment VI, every time $\Omega_{\rm C}$ decreases by κ/R^2 we find the vortex with the maximum radial position $r < R$ and move it outside the container boundary. The wandering vortex motion in experiments V and VI is analogous though not exactly equivalent to vortex creep (Alpar et al. 1984).

We show the evolution of $\Omega_{\rm C}$ in experiments V and VI compared to the result from experiment II in Fig. A6 and summarize the results in Table A2. As shown in Table A2, neither experiment V or VI increases $N_{\rm glitches}$ more than $\approx$30 per cent from experiment II, compared to the $\approx$75 per cent more glitches in experiment I. In fact, we see fewer glitches in experiment VI than in experiment II. A two-sample KS test for the sizes and waiting times in experiments V and VI rejects the null hypothesis that they are drawn from the same distributions as in experiment I, but not in experiment II.

While the idealized vortex wandering algorithms used in experiments V and VI are not exactly equivalent to the addition of vortices at the boundary in experiment I, the results here do suggest that the increase in the number of glitches in experiment I compared to experiment II is not simply the result of perturbations to the vortex array caused by adding vortices randomly, and the interplay of global angular momentum transfer and local pinning dynamics discussed in Section 4.3 remains the most plausible cause.

Table A2. Summary of numerical experiments I, II, V, and VI, showing initial and final numbers of vortices $N_{\rm v,\,i}$ and $N_{\rm v,\,f}$, initial and final container angular velocities $\Omega_{\rm i}$ and $\Omega_{\rm f}$, and number of glitches $N_{\rm glitches}$.

	Experiment I	Experiment II	Experiment V	Experiment VI
$N_{\rm v,\,i}$	1943	1943	1943	1943
$\Omega_{\rm i}/\Omega_0$	1	1	1	1
$N_{\rm v,\,f}$	2361	1498	1492	1336
$\Omega_{\rm f}/\Omega_0$	1.27	0.74	0.74	0.72
$N_{\rm glitches}$	176	101	123	90

This paper has been typeset from a TEX/LATEX file prepared by the author.